Received: 3 December 2022 | Revised: 29 April 2023 | Accepted: 6 June 2023

DOI: 10.1002/jbm.a.37582

RESEARCH ARTICLE

Nanotextured porous titanium scaffolds by argon ion irradiation: Toward conformal nanopatterning and improved implant osseointegration

Ana Civantos[1,2] | Andrea Mesa-Restrepo[3] | Yadir Torres[4] | Akshath R. Shetty[1] | Ming Kit Cheng[1] | Camilo Jaramillo-Correa[1,5] | Teresa Aditya[5] | Jean Paul Allain[1,2,3,5,6]

[1]Department of Nuclear, Plasma and Radiological Engineering, University of Illinois at Urbana-Champaign, Urbana, Illinois, USA

[2]Nick Holonyak, Jr., Micro and Nanotechnology Laboratory, University of Illinois at Urbana-Champaign, Urbana, Illinois, USA

[3]Department of Biomedical Engineering, Pennsylvania State University, State College, Pennsylvania, USA

[4]Department of Engineering and Materials Science and Transport, University of Seville, Seville, Spain

[5]The Ken and Mary Alice Lindquist Department of Nuclear Engineering, Pennsylvania State University, State College, Pennsylvania, USA

[6]Department of Materials Science and Engineering, Pennsylvania State University, State College, Pennsylvania, USA

Correspondence
Andrea Mesa-Restrepo, Department of Biomedical Engineering, Pennsylvania State University, State College, PA 16802, USA.
Email: aqm6463@psu.edu

Funding information
Junta de Andalucía-FEDER (Spain), Grant/Award Number: US-1259771; Ministry of Science and Innovation of Spain, Grant/Award Number: PID2019-109371GB-I00; Pennsylvania State University; University of Illinois at Urbana-Champaign

Abstract

Stress shielding and osseointegration are two main challenges in bone regeneration, which have been targeted successfully by chemical and physical surface modification methods. Direct irradiation synthesis (DIS) is an energetic ion irradiation method that generates self-organized nanopatterns conformal to the surface of materials with complex geometries (e.g., pores on a material surface). This work exposes porous titanium samples to energetic argon ions generating nanopatterning between and inside pores. The unique porous architected titanium (Ti) structure is achieved by mixing Ti powder with given amounts of spacer NaCl particles (vol % equal to 30%, 40%, 50%, 60%, and 70%), compacted and sintered, and combined with DIS to generate a porous Ti with bone-like mechanical properties and hierarchical topography to enhance Ti osseointegration. The porosity percentages range between 25% and 30% using 30 vol % NaCl space-holder (SH) volume percentages to porosity rates of 63%–68% with SH volume of 70 vol % NaCl. Stable and reproducible nanopatterning on the flat surface between pores, inside pits, and along the internal pore walls are achieved, for the first time on any porous biomaterial. Nanoscale features were observed in the form of nanowalls and nanopeaks of lengths between 100 and 500 nm, thicknesses of 35-nm and heights between 100 and 200 nm on average. Bulk mechanical properties that mimic bone-like structures were observed along with increased wettability (by reducing contact values). Nano features were cell biocompatible and enhanced in vitro pre-osteoblast differentiation and mineralization. Higher alkaline phosphatase levels and increased calcium deposits were observed on irradiated 50 vol % NaCl samples at 7 and 14 days. After 24 h, nanopatterned porous samples decreased the number of attached macrophages and the formation of foreign body giant cells, confirming nanoscale tunability of M1–M2 immuno-activation with enhanced osseointegration.

KEYWORDS
argon irradiation, conformal nanopatterning, osseointegration, osteoblast differentiation, porous titanium

1 | INTRODUCTION

Bone tissue's natural ability to repair itself is hindered if the size of the histological defect is greater than about 2 cm. These defects can be caused by trauma, congenital and degenerative diseases, or tumor resection, requiring clinical intervention.[1] For this purpose, titanium (Ti) and its alloys have been used in bone replacement. Despite its high mechanical, physicochemical, and biological properties, monolithic Ti-based metallic biomaterials can trigger chronic inflammation, implant micro-loosening and poor osseointegration after its implantation.[2–4] Moreover, the mismatch in mechanical properties between the bone and Ti bulk implants, results in bone resorption due to insufficient loading. This phenomenon is known as stress shielding and it contributes to the loosening and fracturing of bone implants.[1,5]

Significant efforts have been attempted to develop bioinspired bone substitutes that accomplish several vital requirements: biocompatibility, bioactivity, and having similar mechanical properties as bone tissue.[1] Developing a porous implant materials that mimic the mechanical strength of bone is one strategy to alleviate the stiffness mismatch between the implant and the surrounding bone tissue, preventing stress shielding effects.[5] Several methods have been investigated to produce porous structures such as solid-state replication,[6] freeze-casting,[7] selective electron beam and laser melting,[8] and powder metallurgic techniques.[5] Among these, powder metallurgy (PM) can generate highly porous foams with random and interconnected pores in an accurate, cost-effective, and environmentally friendly manner.[8–11] Using pressure or spacer particles in PM is a low cost and high efficiency method to design controlled porosity Ti scaffolds for dental and orthopedic applications.[5,11,12] Porous Ti synthetized via space holders (SH) results in an interconnected scaffold, which facilitates bone ingrowth and the formation of new blood vessels to irrigate the bone tissue.[11,13]

The extracellular matrix (ECM) is a hierarchical substrate that facilitates cell attachment and provides biochemical and physical cues that regulate cellular processes (migration, proliferation, and differentiation) and tissue homeostasis.[1,14] Bone ECM components range from nano to microscale.[1] Replicating a bone ECM nanoarchitecture into biomaterial surfaces may enhance the biomimetic response by increasing the interaction with progenitor and immune cells.[14–17]

Recent studies inducing nanotopography on biomaterials have shown improved protein adsorption, cell adhesion and differentiation of mesenchymal stem cells, modulation of osteoblast activity, modulation of osteoclast activity and macrophage polarization.[18–21] Several approaches have been used to modify the implant's topography at the micro and nanoscale levels (e.g., anodization, acid etching and grit blasting, plasma spraying, etc.), which have promoted bone formation, each with their advantages and disadvantages.[22–27] Directed irradiation synthesis (DIS) is a direct synthesis process that is eco–friendly, scalable to high-volume, high-value manufacturing by its intrinsic large-area exposure of materials surfaces and interfaces. Furthermore, DIS is a technique that enables nanopatterns to conform to the intrinsic complex geometry of a porous biomaterial, thus providing a conformal nanopatterning along the biomaterial surface. DIS uses energetic ions extracted from low-temperature plasma with controlled beam profiles to introduce surface chemical and topographical changes at micro and nanoscale levels.[28–30] While conventional plasmas are based on the combination of different chemical species (i.e., atoms, ions, electrons, and free radicals), the free radicals can induce changes to a biomaterial when exposed to the atmosphere after processing, and compromising its surface chemistry.[31,32] DIS uses energy and momentum deposition of low-energy incident ions on a material surface to induce nanoscale changes in the surface topography and chemistry. Thus, no free radical is used, and the modifications are stable and permanent. In DIS, energy and momentum deposition from low–energy ions create a damage cascade at the surface of the material, disrupting the crystal lattice of the first few nanometers of the surface. Several ion-induced effects can occur simultaneously, including material surface erosion, surface diffusion, mass redistribution, preferential sputtering due to intrinsic height variations, grain boundaries or composition variations that exist across any realistic surface, and buildup of surface stresses. All these mechanisms synergistically lead to the evolution of patterns whose dimensions and shape depend on ion beam parameters, that is, species, energy, incidence angle, and fluence.[28,33,34] The mechanism behind the nanopatterning process using DIS consists of incident ions enhancing the mobility and diffusivity of surface atoms of the materials combined, under certain cases (depending on DIS parameters) removal of atoms to the gas phase (e.g., surface erosion) resulting in phase separation along the biomaterial surface. Surface diffusivity, mass redistribution, and surface erosion are dependent on energy (e.g., 0.1–10's keV), fluence (e.g., 10^{16}–10^{19} cm^{-2}) and incident angles (normal vs. off-normal).[30,34–36]

In this study, we use DIS with argon (Ar^{+}) ion irradiation of complex porous Ti structures leveraging conformal nanopatterning along surfaces between pores, inside pits, and along the internal walls of pores. The tailored nanotopography is characterized to study how DIS parameters (energy, fluence, and incidence angle) govern the nanopatterning process and control the geometry of the nanotopography on porous Ti biomaterials. Through in vitro cellular experiments, correlations are made with DIS-induced nanopatterns that enable murine osteoblast cells to attach and differentiate. In contrast, lower percentage of attached murine macrophages is observed.

2 | MATERIALS AND METHODS

2.1 | Manufacturing and characterization of porous commercially pure (c.p.) titanium samples

Porous samples have been obtained in this work using the SH technique. Ti powder is mixed with different volume percentages of NaCl (30–70 vol %), using a Turbula® T2C blender for 40 min, to obtain a

good homogenization.[37] Porous titanium samples with varying porosity were obtained using Ti powders produced by a hydrogenation/dehydrogenation process, using c.p. Ti (SE-JONG Materials Co. Ltd., Korea). The chemical composition of the powder was equivalent to c.p. Ti Grade IV according to the ASTM F67-00 standard.[38] The Ti powder size distribution corresponded to 10%, 50%, and 90% passing percentages of 9.7, 23.3, and 48.4 μm, respectively, while the diameter of the spacer particles was $d_{50} = 384$ μm. The homogeneous mixture of Ti and NaCl was compacted at 800 MPa in an INSTRON 5505 machine (Instron, Massachusetts, United States). Afterward, the NaCl spacer was eliminated using the distilled water method (without stirring, at 50°C, for 16 h).[37] Finally, the sintering process was carried out in a molybdenum chamber furnace (Termolab–Fornos Eléctricos, Lda., Águeda, Portugal), at 1250°C for 2 h, under high vacuum conditions ($\sim 10^{-5}$ mbar). The resulting Ti disks (diameter of 12 mm and height of 3 mm) of approximately area of 1 cm^2 were then modified using DIS.

The topography and porosity of porous titanium architectures were evaluated by scanning electron microscopy (SEM, Hitachi 4800), image analysis (Nikon Epiphot microscope and Image-Pro Plus 6.2 software), and high-resolution radiation x-ray-CT (Xradia Bio MicroCT [MicroXCT-400]); porosity parameters (percentage, equivalent diameter and Shape factor) were estimated using the Archimedes' method (ASTM C373-14).[39] Crystallographic information of the surface was examined by grazing angle x-ray diffraction (GI-XRD) with a PANalytical Philips X'pert MRD system with Cu K alpha radiation wavelength ($\lambda = 0.15418$ nm) with generator settings of 45 kV and 40 mA. The 2θ range was set from 20° to 90° and was scanned with a step size of 0.02°. The phase analysis was performed by JADE® software.

Macroscale mechanical behavior of the porous titanium biomaterials was also studied. For this, the yield strength (σy) and dynamic Young's modulus (E_d), were estimated using the uniaxial compression test according to ASTM E9-09 (Instron 5505 universal testing machine)[40] and ultrasound technique (KRAUTKRAMER USM 35), respectively. Micromechanical properties before surface modification were measured by indentation test using Hysitron TI-950 Triboindenter (Bruker, Minnesota, United States) using a standard Berkovich tip calibrated on a fused quartz reference sample and applying a load of 5 mN and analyzed using an Oliver–Pharr model to obtain the Young's modulus. Indentations were performed on a randomly selected location with a spacing of at least 2 μm between indents using a nanoindentation tip as a stylus profilometer with a load of 2 μN.

2.2 | DIS of porous c.p. Ti samples and surface characterization

To carry out the surface modification, porous c.p. Ti samples were subjected to Ar^+ irradiation by DIS. This nanopatterning process was carried out in the Radiation Surface Science and Engineering Laboratory (RSSEL) in the Ion-Gas-Neutral Interactions with Surfaces (IGNIS) facility developed by Allain et al.[28,41] A broad beam of ions was extracted from a microwave electron cyclotron resonance (ECR) plasma source (Tectra Gen II) equipped on IGNIS, with a set of dual extraction grids made of Mo that define ion energy and extract ions from the plasma. Due to the presence of biased grids and the plasma being generated away from the main chamber of IGNIS, the resulting beam should consist primarily of ions. Ion energy (1 keV), fluence or dose (1×10^{18} ions/cm^2), and ion beam incidence angle (0° and 60°) were chosen after a thorough revision of our previous argon irradiation studies on nano-structuring of metallic materials.[28–30,33,42]

After surface modification by DIS, samples were analyzed by SEM, XRD, and x-ray photoelectron spectroscopy (XPS) to evaluate the change at the nanoscale level. Ex situ XPS measurements were carried out in the Kratos Axis ULTRA system at the Frederick Seitz Materials Research Laboratory (FS-MRL). A monochromated, micro-focused Al Kα x-ray source was used. The instrument was also equipped with a low-energy electron flood gun for charge compensation. For each sample, two survey scans and high-resolution scans of the C 1s, O 1s, and Ti 2p photoelectron peaks (10 scans per region) were acquired. Pass energy of 160 and 40 eV were used in the survey and high-resolution scans respectively. In both IGNIS and Kratos systems, the base pressure during analysis was 3×10^{-8} Torr or lower. For non-irradiated Ti surfaces, referred as fully dense (FD) were used as titanium control samples, the binding energy scale was referenced to the C1s peak corresponding to the C—C bond at 284.8 eV. However, since most carbon contaminants were removed by irradiation, samples after irradiation were referenced to the metallic Ti peak of the FD sample instead. Peak deconvolution and calculation of atomic fractions were performed using CasaXPS. A Shirley synthetic background was used. For each chemical species in its respective region, a convoluted Gaussian-Lorentzian function was used for peak fitting. For metallic Ti peak, an asymmetric Lorentzian function was used instead. Relative sensitivity factors (RSF) derived from Scofield photoionization cross sections, provided by SPECS, and empirical RSF provided by Kratos Analytical were used to convert peak areas to atomic fractions. Error analysis of the peak-fitting and atomic ratios was performed using a built-in Monte Carlo procedure in CasaXPS.

2.3 | In vitro cellular experiments

Murine pre-osteoblasts, MC3T3-E1, were purchased from American type culture collection (ATCC, CRL-2593™), to study cell viability, differentiation and mineralization processes. Cell passaging was performed on 25 cm^2 flasks cultured with alpha minimum essential medium (αMEM, Sigma-Aldrich), containing 10% fetal bovine serum (FBS, Thermofisher) plus antibiotics (100 U/mL penicillin and 100 mg/mL streptomycin sulfate, Sigma-Aldrich). Murine macrophages, J774A.1, were purchased from ATCC (CRL-TIB-67™) to evaluate the initial immune response of porous titanium implants. Cellular passaging was carried out on 25 cm^2 flasks with DMEM (Sigma-Aldrich), supplemented with 10% FBS (Thermofisher) plus antibiotics (100 U/mL penicillin and 100 mg/mL streptomycin sulfate, Sigma-Aldrich). Porous titanium substrates were sterilized by autoclave (121°C and 30 min), placed carefully in a 48-well plate and seeded at different cell densities. For cell viability, proliferation, differentiation, and mineralization studies, MC3T3-E1 pre-osteoblasts were seeded at 10,000 cells/cm^2 (10,000 cells per sample). To evaluate the adhesion and morphology of macrophages, J774A.1 macrophages

were seeded at 5,000 cells/cm^2 (5,000 cells per sample). The cell densities of 10,000 or 5,000 cells/cm^2 are based on the surface area of the top of the Ti discs, which have a diameter of 12 mm, equivalent to 1 cm^2. This approximation assumes that the top surface of the Ti discs can be considered as a circular shape, allowing us to maintain a consistent and comparable cell density across samples. However, it's important to note that this calculation does not take into account the porosity of the Ti samples, and further studies may be needed to evaluate the potential impact of porosity on cell densities. FD were used as titanium controls.

2.3.1 | Osteoblast cell viability

To determine if the surface treatment causes cell death of osteoblasts, the percentage of live cells or the relative cell viability was determined via AlamarBlue® assay (Invitrogen). AlamarBlue assay is based on the reduction of resazurin to its fluorescent form (resorufin) by metabolically active cells; thus, the quantity of produced resofurin is related to the number of viable cells. Briefly, after 24 h in culture with the MC3T3-E1, porous metallic samples were transferred to a new 48-well plate with fresh media (400 µL) and 40 µL of AlamarBlue® reagent for 1 h 30 min at 37°C in the dark. After that, samples were removed, and the fluorescence signal was read using a micro-plate reader (Synergy HT Biotek) with filters ($\lambda_{ex}/\lambda_{em}$ 535/590 nm). The resulting fluorescence of the porous samples was normalized to the FD fluorescence to obtain the relative percentage of viable cells on the surfaces.

2.3.2 | Osteogenic differentiation: Quantification of ALP activity

MC3T3-E1 were seeded onto porous titanium samples with osteogenic media for 7 and 14 days. The osteogenic media contains α-MEM medium supplemented with 50 µg/mL ascorbic acid (Sigma Aldrich), 100 nM of dexamethasone (Sigma Aldrich) and 1 mM of β-glycerophosphate (Sigma Aldrich) to induce osteoblast differentiation. Cell media was changed every 2 days and at day 7 and day 14 alkaline phosphatase activity (ALP) was quantified using an ALP kit (Abcam, ab83369) based on the manufacturer's instructions. In short, samples were washed with phosphate buffer saline (PBS), lysed with the kit's buffer and subjected to three freeze–thaw cycles of (−80°C) and (37°C) for 30 min each step. Then, we measured the absorbance at 405-nm using a microplate reader (Synergy HT, Biotek). ALP results were expressed as nmol/min/mL.

2.3.3 | Cell mineralization: Evaluation of calcium deposits

MC3T3-E1 cell line was seeded onto porous Ti samples with osteogenic media changed every 2–3 days. At 14 days, the samples were washed with PBS, fixed with 4% formaldehyde for 15 min, stained with 40 mM of alizarin red solution (Sigma Aldrich) for 30 min and washed 5 times with deionized water. Images were taken using an optical microscope. To quantify the staining, the samples were placed in a 24-well plate with 10% acetic acid solution and then we measured the absorbance at 405-nm.

2.3.4 | Macrophage adhesion: Morphological evaluation and relative cell attachment quantification

Cytoskeletal organization of macrophages J774A.1 was studied at 24 h. In short, cells were rinsed twice with PBS, fixed in 4% paraformaldehyde, permeabilized in 0.1% buffered Triton X-100 0.1% and cell cytoskeletal filamentous actin (F-actin) was visualized using Texas red phalloidin (Molecular Probes) while the nuclei were stained using Hoechst (Thermofisher). Later, samples were washed with PBS and images were obtained using confocal microscopy (Leica). AlamarBlue assay was used to evaluate macrophage adhesion after 24 h on the porous samples (see Section 2.3.1). The resulting fluorescence of the porous samples was normalized to the FD fluorescence to obtain the relative percentage of viable cells attached to the surfaces.

2.4 | Statistical analysis

All experiments were carried out as three independent experiments. Data were expressed as mean ± SD. One-way analysis of variance and Tukey post treatment were applied to evaluate the data for significant differences (p value <.05) using OriginPro 2022 software.

3 | RESULTS

Figure 1 summarizes the SEM images of porous Ti-based scaffolds evaluated in this study, with varying volume percentage of NaCl as the spacer particle (30–70 vol %). At the microscale level, the SEM micrographs show the complex micro-topography generated by the SH technique. The pores, which exhibit a quasi-square shape, follow a bimodal size distribution, with two main average pore sizes: 158 ± 58.8 µm referred as big pores and 30 ± 8.9 µm called small pores (red and white arrows, respectively). The small pores are inherent of the sintering process and removal of the spacer, while the big pores are associated with the percentage and range of particle sizes of the spacer used.

The surface microstructure and chemistry were analyzed by XRD and in situ XPS. Figure 2 shows the results of XRD. In the XRD pattern, we observe the peaks corresponding to pure crystalline Ti in the α-phase, which is the most stable phase at room temperatures and below 882°C, having a hexagonal close packed structure. These peaks are located at $2\theta = 35°$, 37.5°, 40°, 53°, 63°, 70.5°, 76°, 77.5°, 87° corresponding to the values of the plane (100), (002), (101), (102), (110), (103), (112), (201), and (004).[43,44] The XPS analysis of the porous surfaces, revealed the presence of the contaminants such as:

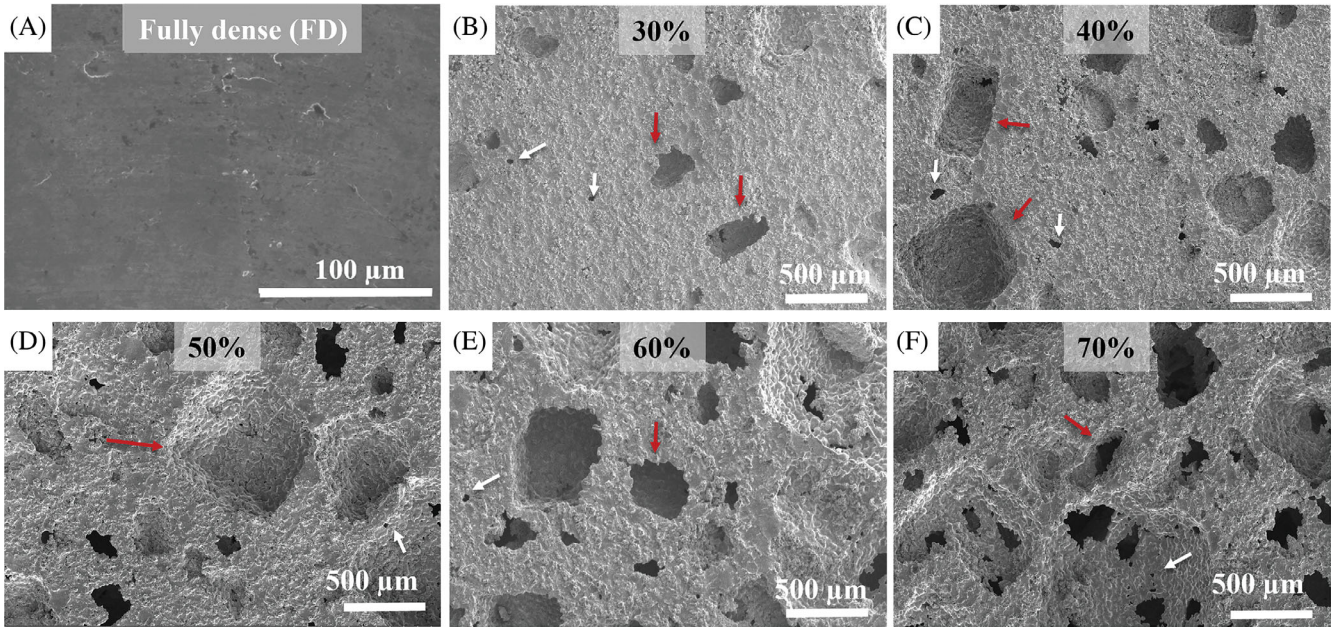

FIGURE 1 Scanning electron microscopy (SEM) of porous Ti scaffolds generated via space holder technique using different percentages of NaCl. Fully dense (FD) are fully dense Ti scaffolds developed via powder metallurgy. Red arrow indicates large pores (158 ± 58.8 µm) while white arrows indicate small pores (30 ± 8.9 µm).

FIGURE 2 X-ray diffraction (XRD) characterization of porous Ti scaffolds generated via space holder technique using different percentages of NaCl.

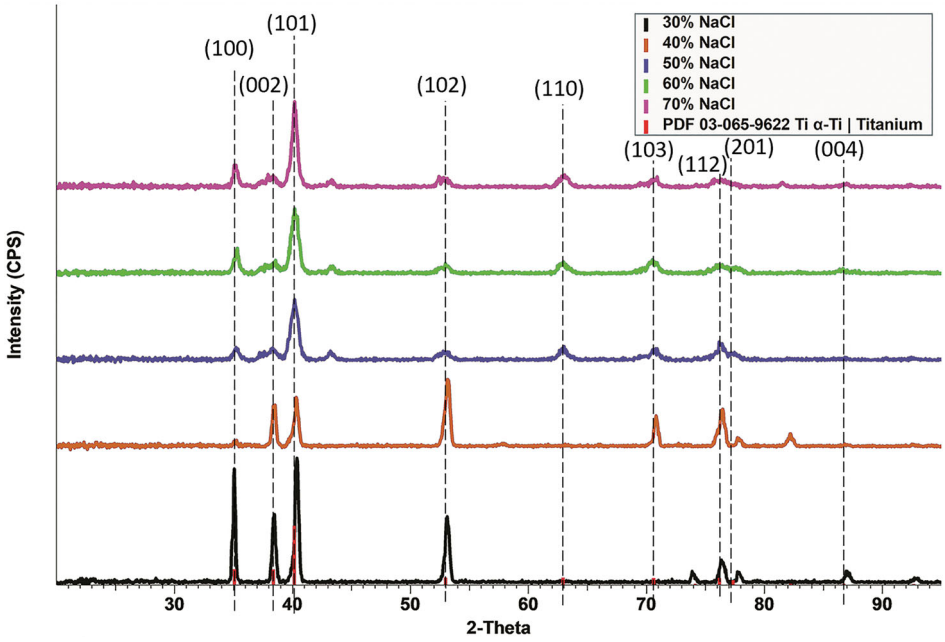

Zn, Na, and F, which are likely related to the sintering process including small fragments of spacer particles left after the removal of the spacer during the fabrication process (see Figure 3 and Table 1).

The increased percentage of spacer particles affects the total and interconnected porosity as well as the mechanical properties of porous scaffolds. For that reason, computerized micro-tomography (micro-CT) and indentation tests were performed to analyze these properties. The porosity results are compiled in Figure 4 and Table 2. The 3D reconstruction micro-CT images revealed the same pore morphology observed in SEM; however, the resultant total porosity achieved was slightly lower (23.46%, 40.58%, and 62.55%) compared to the theoretically designed values of 30, 50, and 70 vol %, respectively. This reduction is based on the limitation of the image analysis via micro-CT, and it has been reported in other studies using similar methods to determine the same property.[5,12,45] Porous samples with high interconnected porosity offer a great network for the development of bone ingrowth and a new vascularized system to irrigate.[11,13] In this study, we observed an increased interconnected porosity in

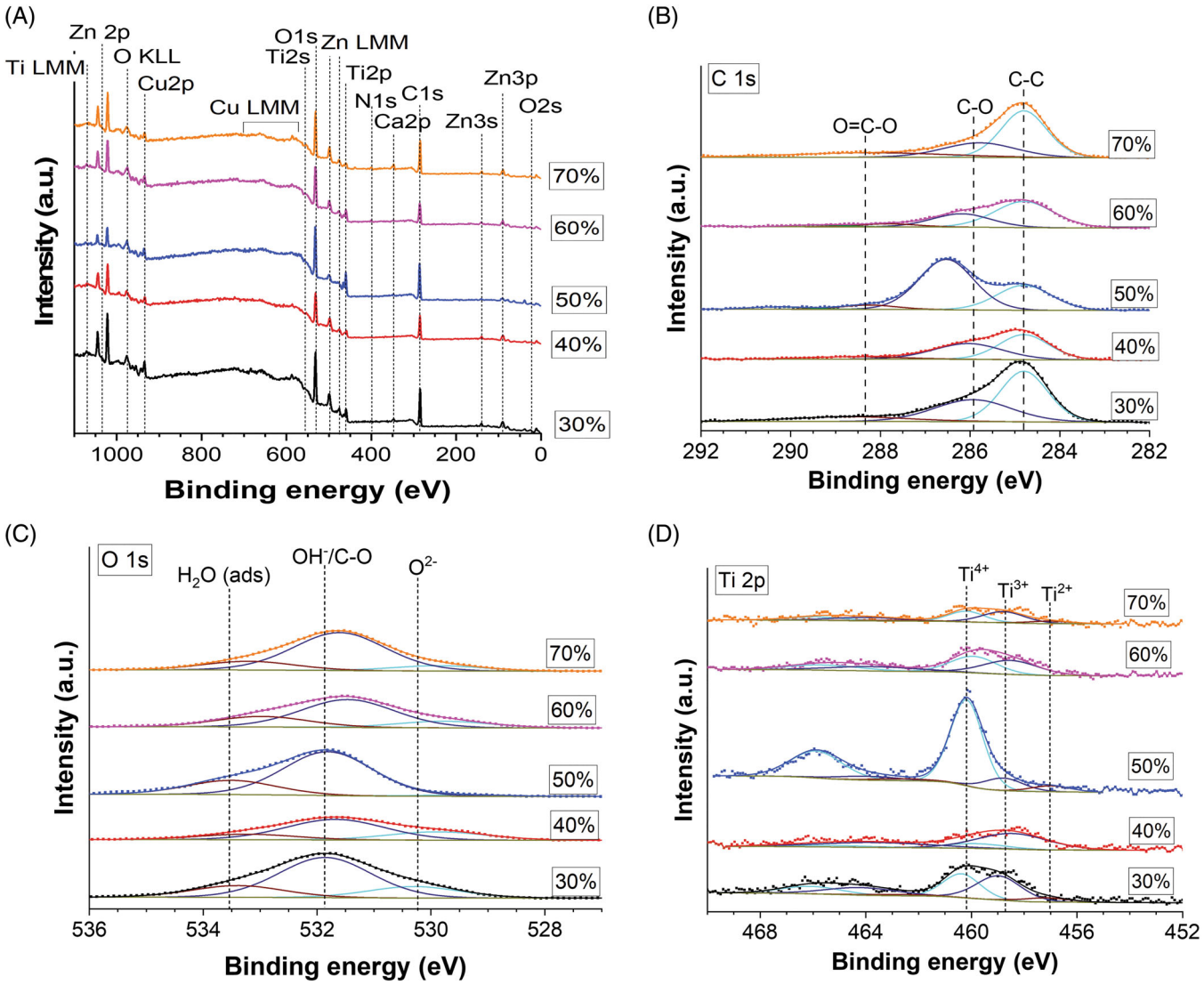

FIGURE 3 X-ray photoelectron spectroscopy (XPS) analysis of porous Ti samples generated via different percentage of NaCl. The survey scan is observed in (A), and analysis of C1s, O1s, and Ti2p regions can be observed in (B), (C), and (D), respectively.

TABLE 1 XPS derived chemical analysis of porous Ti samples generated via different percentage of NaCl.

		Spacer particle percentage				
Chemical element		**30 vol %**	**40 vol %**	**50 vol %**	**60 vol %**	**70 vol %**
Atomic fraction (%)	C	60.66 ± 0.54	61.85 ± 0.71	63.02 ± 0.50	55.49 ± 0.73	62.65 ± 0.56
	O	28.12 ± 0.48	29.23 ± 0.63	28.15 ± 0.46	33.63 ± 0.64	27.64 ± 0.47
	Ti	2.80 ± 0.18	3.18 ± 0.21	5.79 ± 0.21	4.26 ± 0.22	1.00 ± 0.13
	Cu	2.91 ± 0.19	1.06 ± 0.15	1.01 ± 0.10	1.15 ± 0.12	0.93 ± 0.10
	Zn	4.85 ± 0.14	4.68 ± 0.18	1.65 ± 0.12	4.38 ± 0.16	4.17 ± 0.13
	Ca	0.66 ± 0.12	Undetectable	0.37 ± 0.09	Undetectable	1.59 ± 0.16
	N	Undetectable	Undetectable	Undetectable	1.09 ± 0.41	2.02 ± 0.37

Abbreviation: XPS, x-ray photoelectron spectroscopy.

those samples with a higher amount of spacer particles, being the highest in 70 vol % NaCl porous Ti, where we observed pore coalescence. Nevertheless, high interconnectivity has been associated with poor mechanical properties,[5] which 70 vol % NaCl porous substrates showed in the mechanical tests (0.45 GPa, see Table 3). As seen in Table 3, the mechanical stiffness of FD samples (~101.2 ± 0.3 GPa) is

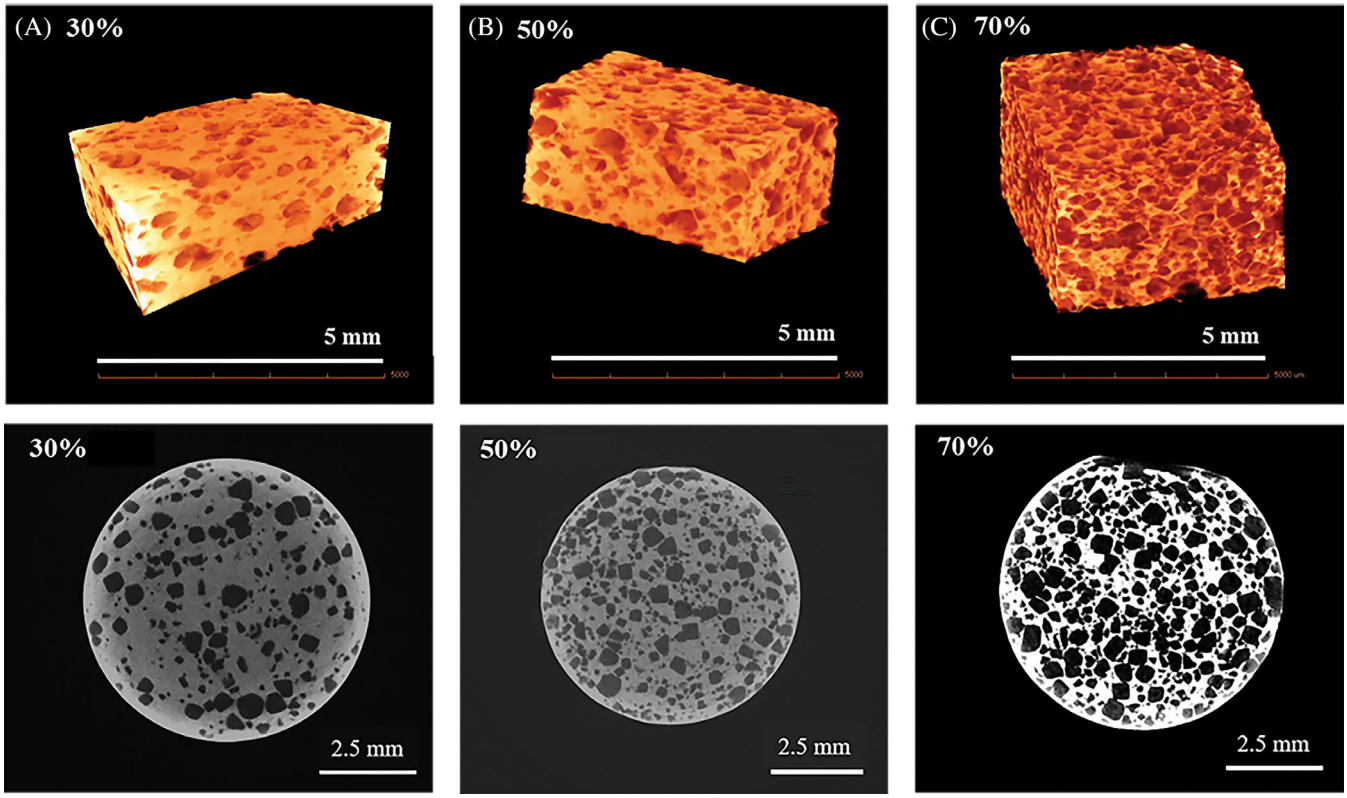

FIGURE 4 Micro-CT images of porous titanium scaffolds with 30%, 50%, and 70% NaCl.

TABLE 2 Results of microstructural characterization of porosity designed.

Manufacturing route		Porosity percentage (%)			Equivalent diameter (μm) Image analysis	Shape factor[a]
PM conventional	Fully dense	Archimedes method 2.6	Image analysis 2.3	Micro-CT –	8	0.91
SH	30 vol %	27.7 ± 0.6	32.1 ± 0.5	23.46	210 ± 12	0.75 ± 0.1
	40 vol %	37.4 ± 0.5	38.5 ± 0.6	–	240 ± 15	0.82 ± 0.2
	50 vol %	47.8 ± 0.6	51.3 ± 0.6	40.58	298 ± 13	0.71 ± 0.1
	60 vol %	57.1 ± 0.8	58.0 ± 0.7	–	312 ± 19	0.62 ± 0.2
	70 vol %	68.3 ± 1.0	66.9 ± 0.9	62.55	351 ± 24	0.81 ± 0.2

Note: Parameters of the porosity percentage, equivalent diameter, and shape factor were evaluated.
Abbreviations: PM, powder metallurgy; SH, space-holder.
[a]$F_f = 4\pi A/(PE)^2$, where A is the pore area and PE is the experimental perimeter of the pore. At least three measurements have been made for each material and type of test. Data shows mean ± SD.

higher compared to cortical bone's (~25 GPa) and trabecular bone tissue (0.5–1 GPa).[11,46,47] This great difference is one of the main causes of stress shielding, which derives from a stiffness mismatch that induces bone resorption and can cause implant failure.[1,5] In contrast, the Young modulus of 50 vol % and 60% porous samples (2.32 and 3.97 GPa, respectively), were closer to trabecular bone young modulus. Thus, by varying the porosity, the stiffness of the porous scaffolds can be adjusted, making them more suitable for bone tissue regeneration applications.

Considering the scaffolds' mechanical properties and interconnected porosity, 50–60 vol % NaCl porous Ti samples were chosen for the in vitro experiments.

The main goal of the study was to create a hierarchical structure, mimicking the bone ECM environment, to enhance implant's osseointegration and complement the biomechanical properties of the porous Ti structure. This was achieved by nanopatterning porous Ti architecture by DIS. DIS parameters such as incidence angle and energy were studied to evaluate their influence in surface nanotopography (i.e., nanofeature size, nanopattern conformation, and geometry). Figures 5, 6, S1, and S2 summarize the SEM images of porous scaffolds before and after DIS irradiation on the same region, using Ar^+ ions, energy (1 keV), fluence (1×10^{18} ions/cm^2), and normal (0° or 0°) and off-normal (60° or 60°) incidence angle. Complex morphologies were found over various

TABLE 3 Macro and micromechanical behavior of the studied materials before DIS surface treatment.

Sample name		Young's modulus (GPa)			
PM conventional	Fully dense	Nanoindentation –	Ultrasound technique 98 ± 2	Uniaxial compression tests 70 ± 0.5	Yield strength, σ_y (MPa)[a] 630 ± 8
SH	30 vol %	6.38	45.4 ± 0.5	4.5 ± 1.0	415 ± 10
	40 vol %	6.19	29.7 ± 0.7	5.4 ± 1.1	263 ± 12
	50 vol %	2.32	24.2 ± 0.6	4.1 ± 0.9	192 ± 14
	60 vol %	3.97	17.9 ± 0.8	3.7 ± 0.8	100 ± 7
	70 vol %	0.45	8.1 ± 1.2	2.2 ± 1.5	87 ± 10

Note: At least three measurements have been made for each material and type of test. Data shows mean ± SD.
Abbreviations: DIS, direct irradiation synthesis; PM, powder metallurgy; SH, space-holder.
[a]Via uniaxial compression test.

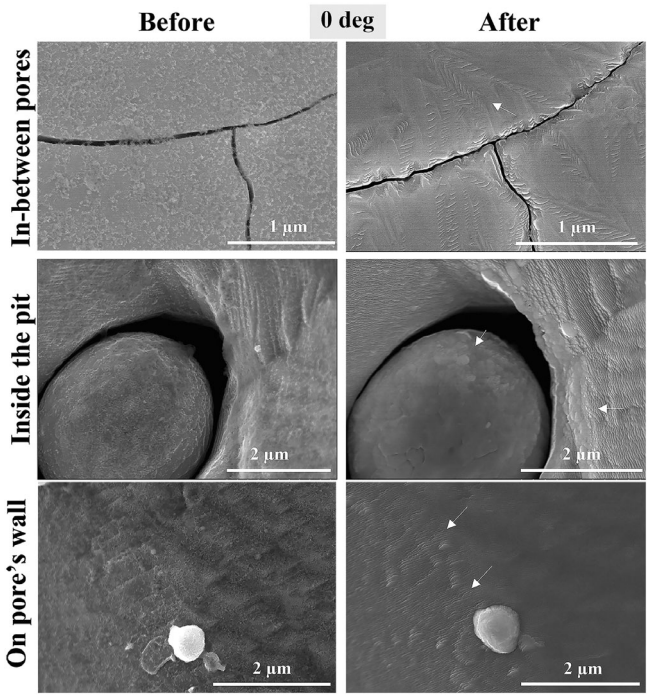

FIGURE 5 Scanning electron microscopy (SEM) images of porous titanium generated with 50%–60% of NaCl before and after treatment with 1 keV Ar^+ ions at a dose 1×10^{18} ions/cm^2 and 0° incidence angle. The white arrows indicate direct irradiation synthesis (DIS) *conformal nanopatterning* of three primary regions: (1) in-between pores surfaces, (2) inside pits, and (3) on the pore's wall.

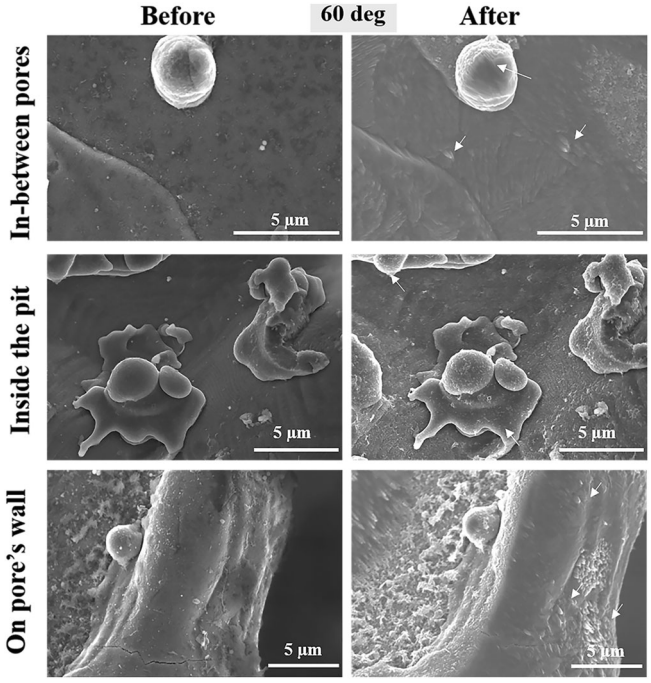

FIGURE 6 Scanning electron microscopy (SEM) images of porous titanium generated with 50%–60% of NaCl before and after treatment with 1 keV Ar^+ ions at dose 1×10^{18} ions/cm^2 at 60° incidence angle. The white arrows indicate direct irradiation synthesis (DIS) *conformal nanopatterning* of three primary regions: (1) in-between pores surfaces, (2) inside pits, and (3) on the pore's wall.

locations of the porous Ti surfaces. The nanotextured locations vary from flat areas between pores, round microstructures, inside pits, and along the internal walls of pores. As these SEM images manifest, we could compare the Ti surface modification in the same exact location before and after argon irradiation, highlighting the versatility of DIS. Three different locations, (i) regions between pores (also referred as flat surface), (ii) inside pits (i.e., defined as pores with large diameter but shallow depth where the diameter of the pore is ≫ than the depth of the pore and not interconnected), and (iii) along a pore's inner walls were examined by SEM. At a normal incidence angle (0°) the irradiation resulted in a more homogeneous surface nanotopography covering the entire surface including inside pores, artifacts, and cracks (previously presented before irradiation). Thus, the ion-irradiation using DIS can conform to any geometry (*conformal nanopatterning*), which allows us to generate nanopatterns of order <100-nm on complex geometries, for example, jagged edges, plates, as well as porous materials used in bone tissue engineering applications. This is critical to the functional effect of nanopatterns on microscale pores in these Ti-based materials.

Comparing Figure 6 with 5 we found that increasing the angle of incidence results in different nanopatterns due to changes in ion orientation and their interaction with the complex porous structure.

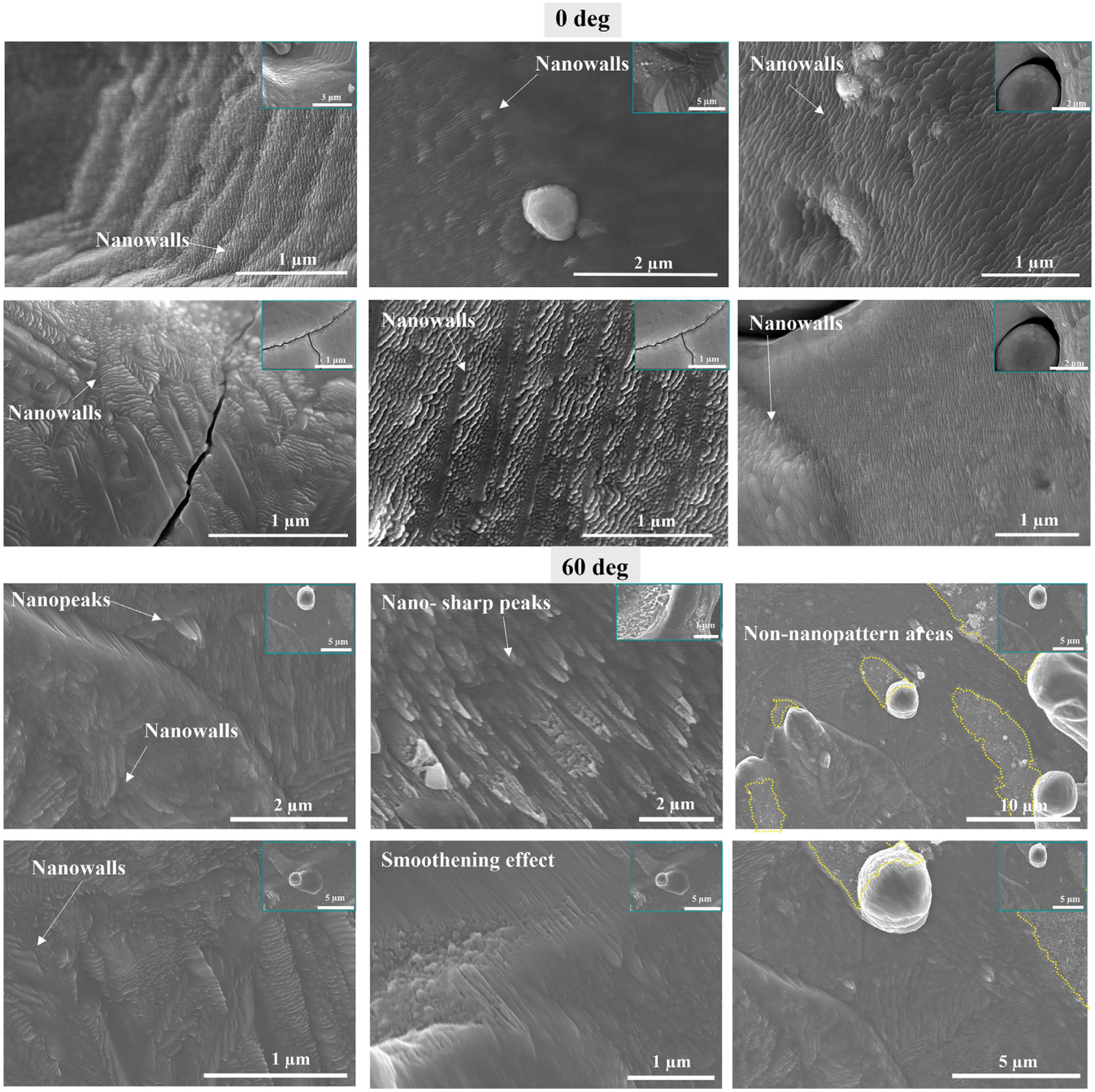

FIGURE 7 Scanning electron microscopy (SEM) of nanopatterned porous titanium treated with 1 keV Ar^+ ions at a dose of 1×10^{18} ions/cm^2 at 0 and 60° incidence angle zoom out from the images on the right (blue). The yellow area indicates areas that are not patterned.

Predominant nanowalls (thickness of 35.7 ± 19.7 nm) are nanopatterned when using 0°. Similarly, 60° tailored larger nanowalls (thickness of 39 ± 22.24 nm) and nanopeaks (length of 90.7 ± 66.76 nm) compared to 0°. Ar^+ ions inside the pore will hit line-of-sight wall surfaces and then reflect to the nearby wall surfaces with a different incidence angle and lower energy, which has been reported by Allain et al. in magnesium porous samples.[48] This leads to nanopatterning along a pore wall, although some SEM images did not allow to focus with high resolution enough to detect these nanofeatures presented in Figure 7. It should be highlighted that the scaffolds irradiated at off-normal incidence angle exhibit a wider variety of nanofeatures including nanowalls, nanopeaks, and smooth nanopattern areas. It has been observed that disordered nanostructures can induce the osteogenic differentiation of osteoprogenitors cells.[49] Thus, the DIS conditions with Ar^+ ion irradiation at 60° incidence angle of the porous Ti samples were preferred.

These SEM micrographs confirm that the incidence angle can tailor nanowalls and nanoripples in regions between pores and inside pit surfaces. However, there is a predominant morphology of rounded nanofeatures versus nanopeaks or nanocones using normal and

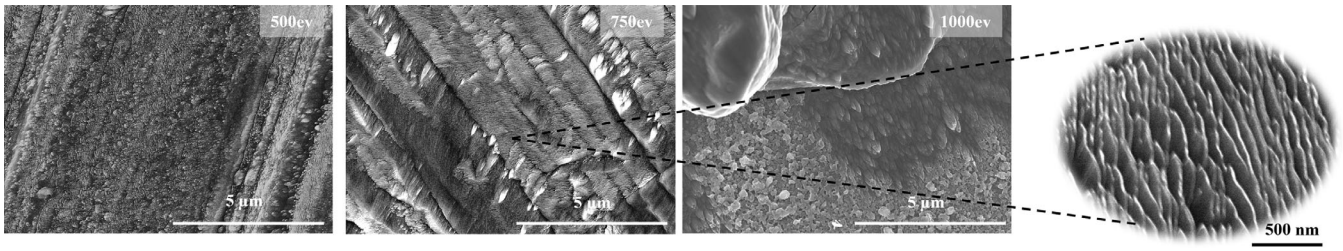

FIGURE 8 Scanning electron microscopy (SEM) of nanopatterned porous titanium treated with Ar^+ ions at a dose of 1×10^{18} ions/cm^2 at 60° incidence angle for energies: 500, 750, and 1000 eV. Higher magnification region for the 750 eV case shows that nanowall pattern structure is prevalent at energies lower than 1000 eV (e.g., at 750 eV).

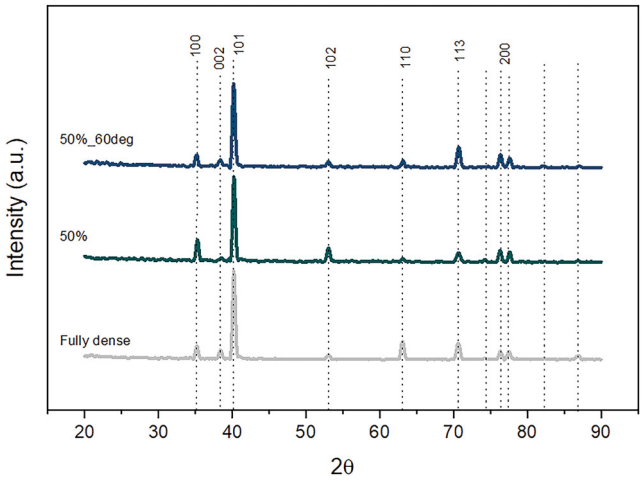

FIGURE 9 X-ray diffraction (XRD) characterization of nanopatterned porous titanium generated with 50% NaCl (i.e., treated with 1 keV Ar^+ ions at a dose of 1×10^{18} ions/cm^2 at 60° incidence angle).

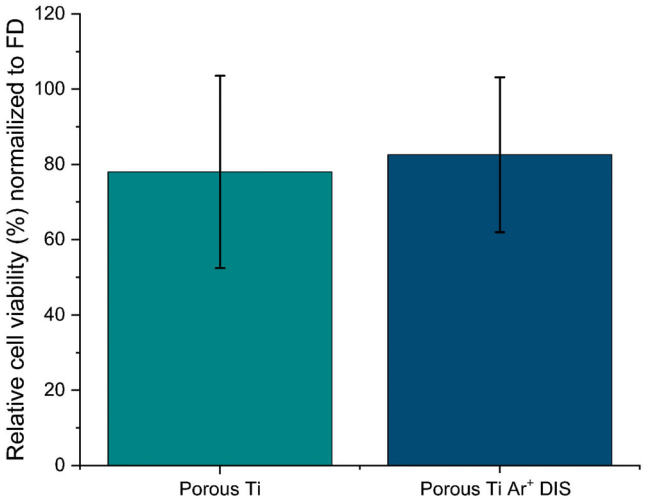

FIGURE 10 Cell viability of pre-osteoblasts on nanopatterned porous titanium treated with Ar^+ ions via direct irradiation synthesis (DIS) after 24 h in cell culture normalized to fully dense (FD). $N = 3$ independent experiments, Mean ± SD, analysis of variance.

off-normal incidence angles, respectively. Similarly, the incident Ar^+ energy was varied to evaluate the influence on the nanopatterning process using 500, 750, and 1000 eV shown in Figure 8. Lower energy regimes induce smaller and less-ordered nanofeatures than higher energies (e.g., 1 keV). Lower incident energies result in shallower collision cascades and lower mobility and diffusivity of surface atoms, which can explain the lack of observed ordered nanotexture.

In addition to ion-enhanced surface diffusivity, the removal of surface atoms via sputtering can also tune the surface nanotexture. Furthermore, higher reflected energies can also help induce and proliferate nanotexture inside pores. While sputtered atoms can be removed on flat and open surfaces, inside the pore the collision cascade which depends on the ion energy, fluence, and incidence angle, could generate different nanopatterns compared to the topography observed at the surface.[30,34–36] However, with this treatment the crystalline structure of the samples remains similar to the XRD shown in Figure 9, thus demonstrating that the DIS is a surface-limited material modification that keeps the crystalline structure of the bulk Ti material intact.

The biological response of the surface nanotopography was further studied through in vitro tests designed to investigate cell expression linked to related bone formation behavior. The relative cell viability is defined by the percentage of live pre-osteoblasts cultured for 24 h in the 50% of NaCl porous samples (Porous Ti) and 50% of NaCl porous samples irradiated with 1 keV Ar^+ ions at a dose of 1×10^{18} ions/cm^2 at 60° incidence angle (porous Ti Ar^+ DIS) compared to FD samples and is shown in Figure 10. We did not observe a significant decrease in cell viability between porous samples with or without Ar^+ treatment and control FD samples at the early stages of cell attachment.

Nanofeatures that mimic the native ECM have promoted cell attachment, osteogenesis and vascularization.[20,30] In this context, ALP enzyme, an early bone differentiation marker expressed by osteoblastic cells[50,51] on these irradiated porous substrates was evaluated at 7 and 14 days. On day 7, ALP activity increases on porous Ar^+ irradiated samples and their non-irradiated counterparts compared to FD (Figure 11A). On day 14, the ALP activity of the FD samples tends to be higher than the porous samples (Figure 11B). Osteogenic progenitors decrease their proliferation rate in favor of differentiation, of which ALP is an early marker as it is involved in the synthesis of

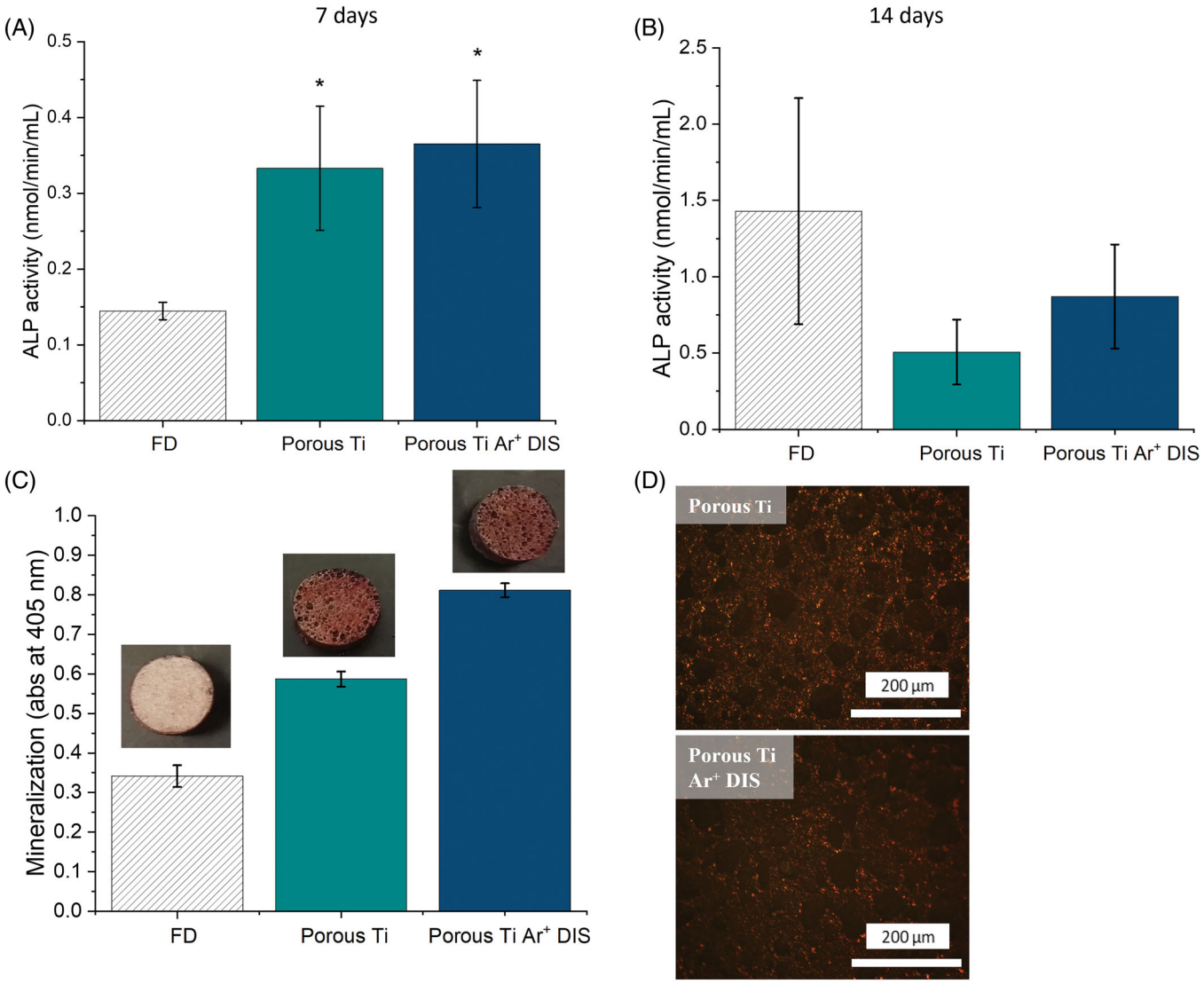

FIGURE 11 Pre-osteoblast cell differentiation and mineralization on nanopatterned porous titanium treated with Ar^{+} ions via direct irradiation synthesis (DIS). (A) Alkaline phosphatase (ALP) activity after 7 days in culture, $N = 3$ independent experiments, Mean ± SD, analysis of variance (ANOVA), Tukey, $^{*}p < .05$ compared to FD. (B) ALP activity after 14 days in culture, $N = 3$ independent experiments, Mean ± SD, ANOVA, Tukey, $^{*}p < .05$. (C) Alizarin red quantification of cellular mineralization after 14 days in culture, Representative of three independent experiments, Mean ± SD. (D) Micrographs of the porous scaffolds during the mineralization test, red coloration corresponds to calcium deposits. Scale bar equivalent of 200 µm.

inorganic phosphates to form hydroxyapatite. Thus, it is present in the maturation and the beginning of the mineralization stages of osteoblast differentiation.[50,51] To evaluate the final stage of mineralization by mature osteoblasts[51] we used Alizarin red to quantify calcium nodule production on the surfaces (Figures 11C and S3), which appears to be higher in Porous Ti Ar^{+} DIS samples compared to FD samples. The optical images in Figure 11D indicated evidence of red deposits localized on the porous surfaces, compared to FD.

The immune system plays a critical role in bone repair. Macrophages communicate with osteoblasts, and osteoclasts via cytokine, chemokines, and other signal molecules.[52] Once the biomaterial is implanted, it is recognized by immune cells (e.g., neutrophils and macrophages). Recruited macrophages express a pro-inflammatory M1 phenotype. These cells secrete cytokines (interleukin 1(IL-1), tumor necrosis factor (TNF-α), and interleukin 6 (IL-6)) to eliminate the source of inflammation, for example, implant. Failure to resolve the inflammation (chronic inflammation) leads to bone resorption and finally implant rejection.[53,54] However, if M1 macrophages switch to an M2 phenotype and express anti-inflammatory cytokines (interleukin 10 [IL-10], interleukin 4 [IL-4]) and tissue repair growth factors (transforming growth factor-β, TGF-β), then bone formation can be promoted.[52–55] Macrophages can sense and adapt to the physicochemical cues in their environment; thus, by tailoring the surface topography, chemistry, stiffness, or wettability we can modulate the foreign body response and rate of tissue inflammation.[53,54,56] Figure 12 shows macrophage response to the nanotextured porous

scaffolds. We observed that the Porous Ti Ar^+ DIS samples decrease macrophages viability compared to FD after 24 h, possibly by promoting macrophage clearance (Figure 12A). Regarding cell morphology at 24 h, the cells expressed low actin fibers (in red color) in all surfaces. We observed macrophages with two to three cell nuclei inside FD and porous titanium, yet we did not observe this phenomenon on Porous Ti Ar^+ DIS samples (Figure 12B). The presence of multiple nuclei could potentially lead to the formation foreign giant cells, which are fused macrophages with hundreds of nuclei. These cells are present in chronic inflammatory reactions, leading to fibrous capsule formation and might contribute to aspect loosening by leading osteoclast bone resorption.[56,57] However, further experiments are needed to further evaluate macrophage polarization and switch to a more tissue regenerative phenotype (M2).

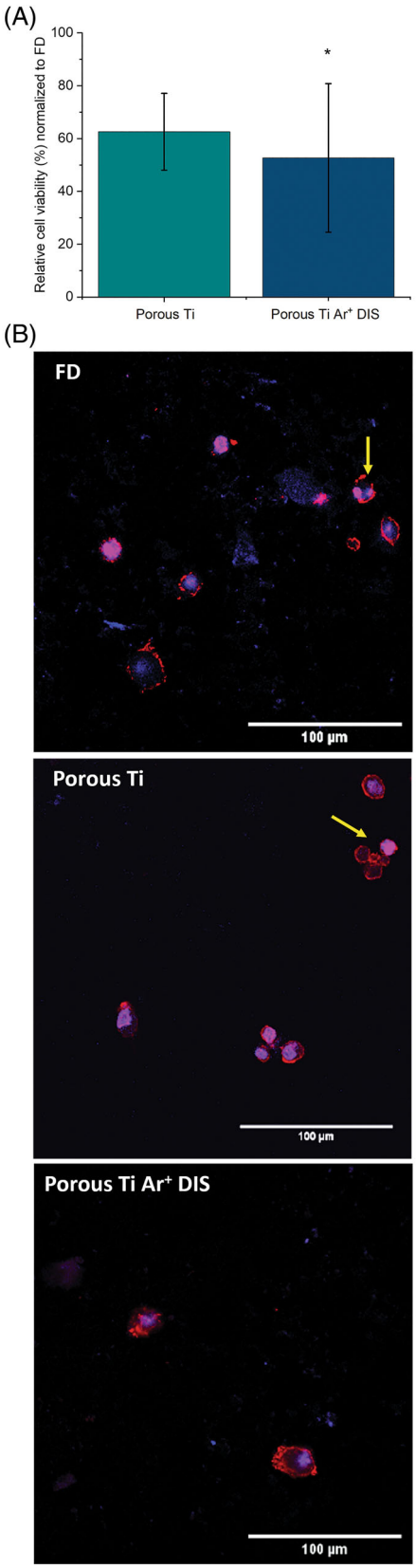

4 | DISCUSSION

The pore size and the interconnectivity of pores are two vital physical aspects essential for healthy bone reconstruction and are controlled by the type of spacer particles used.[5,58] Our porous titanium scaffolds with interconnected pores of 158 ± 58.8 µm promoted bone formation (Figure 11). Small pores (less than 100 µm) favor non-mineralized bone formation whereas large pores (equal or more than 200 µm) promote the formation of mineralized matured bone tissue. In addition to promoting new bone in-growth, large pores allow macrophage infiltration, bacterial clearance and facilitate the formation of a new vascularized system that is essential to enrich, with blood and nutrients, the new bone ECM.[58] Other studies have shown that porous scaffolds with a pore size range between 100 and 400 µm provide higher mechanical strength and stability to promote bone ingrowth, which could enhance osseointegration.[8,11,49,59,60]

Numerous studies have pointed out the role of nanotopography on cell/matrix/substrates interactions. Nanofeatures of 10–100's nm order are in the same scale as cell receptors (e.g., integrins). Cells interact with nanoscale components of their ECM via filopodia (protrusions) which contain integrins. These interactions activate signaling cascades that modulate cellular process, for example, proliferation, migration, and differentiation.[20,30] Previous results in our group demonstrated increased filopodia density and length when interacting with Ar^+-treated nanopatterned titanium alloy (Ti6Al4V) substrates.[30] The characteristics of porous materials (e.g., total and interconnected porosity percentage) affect the expression of osteogenic markers like ALP,[11] which increased for the porous scaffolds after 7 days and promoted surface mineralization after 14 days. Based on the 7 days ALP and 14 days mineralization results in Figure 11, we conjecture the

FIGURE 12 Macrophage attachment on nanopatterned porous titanium treated with Ar^+ ions via direct irradiation synthesis (DIS). (A) Cell adhesion measured as relative percentage of viable cells present after 24 h in cell culture normalized to fully dense (FD). $N = 3$ independent experiments. Mean ± SD. analysis of variance, Tukey. *$p < .05$ compared to FD. (B) Immunostaining of macrophages on nanopatterned porous Ti, nuclei in blue, actin filaments in red, yellow arrows indicate multinucleated cells.

increase in ALP activity for FD samples after 14 days in Figure 11B is due to the increase in cell proliferation of pre-osteoblasts and their late differentiation into mature osteoblasts compared to porous samples, which started the mineralization process a week earlier. This conjecture is supported by evidence shown in Figure 11C,D showing convincing results of a mature mineralization process compared to the FD samples.

The induction of osteoblast differentiation and mineralization on nanotextured porous samples are consistent with the results reported in other studies. For example, Rosa and coworkers observed that porous Ti discs (pore size between 50 and 400 μm and a total porosity of 60%) fabricated by powder metallurgy induced cell differentiation and mineralization of osteogenic cells obtained from human alveolar after 17 days.[61] Abagnale and collaborators observed that micro or nano-patterns generated on polyimide material using reactive ion etching or multi-beam laser interference, respectively, modulate MSC differentiation into osteogenic or adipogenic lineages. Ridges of 15 μm induced adipogenic differentiation, whereas 2 μm ridges enhanced osteogenic differentiation. Notably, nano-patterns with a periodicity of 650 nm increased differentiation toward both osteogenic and adipogenic lineages under specific differentiation media.[62] Tan and coworkers further enhanced the biological properties of acid-etched microrough titanium surfaces by generating titania nanotextured thin films (roughness of 106.9 nm) via chemical oxidation. Nanopatterning of microrough titanium surfaces led to improved attachment and proliferation of MSCs, osteoblast differentiation and mineral deposition.[63] These studies and ours, are limited since they were conducted in static in vitro cultures, which cause hypoxia due to deficiencies in nutrient transport.[64] Moreover, they do not include co-culture with other cells nor mechanical stimulation which does not reflect reality. Thus, for future experiments we will study the response to modified porous Ti surfaces in a dynamic environment. Bacterial attachment is another concern for high-contract area porous Ti samples.[65] The added nanotopography from DIS treatment could be used strategically to address this, as nanostructured Ti surfaces have been able to decrease bacterial attachment.[66] Surface modification with DIS of bacterial cellulose has demonstrated a decrease E. coli and S. Aureus attachment to cellulose-based surfaces.[67] Although further studies are needed studying DIS-nanopatterned porous Ti surfaces, this approach can provide a possible solution to concerns with bacterial attachment in porous Ti materials.

Several authors have observed a change in cell behavior correlated to the nanopatterning in diverse materials. For example, Padmanabhan and coworkers generated nanopattern arrays (55 nm nanorods) on bulk metallic glasses that restricted cytoskeletal remodeling-associated signaling, reducing macrophage fusion.[56,68] Also, Karazisis and coworkers described the reduction of TNF-α expression and osteoclasts markers after 3 and 6 days, respectively, when macrophages were cultured onto highly ordered nanopatterned (79 nm) titanium implant. This effect appeared to be independent of the underlying microscale topography.[16] Chen and coworkers generated ordered and uniform porous anodic alumina with 15, 50, 100, and 200 nm pore sizes. Cells cultured on 0–100 nm substrates were rounded while cells grown on 200 nm structures were less round and have more filopodia. The 100 and 200 nm substrates seemed to be the most anti-inflammatory. In terms of osteogenesis and osteoclastogenesis, 50 and 100 nm nanopatterned surfaces induced the secretion of osteogenic factors (TGF-β, bone morphogenic protein [BMP], vascular endothelial growth factor [VEGF]) while 200 nm surfaces inhibited osteoclasts activity.[21] This osteoimmune environment is indispensable for bone formation via the osteogenic differentiation of osteoblastic lineage cells during the regenerative process.[53] Since nanotopography is associated with osteogenesis, the immune response should be considered in the rational design of suitable surface properties on porous Ti scaffolds.

Civantos and collaborators observed the expression of C-C motif receptor 7 (CCR7) (M1 surface cell marker) on FD surfaces. However, 50% ammonium bicarbonate and hydrofluoric acid generated a CCR7 negative modified porous sample that was more biomimetic than FD surfaces.[11] Although future work is needed to determine macrophage polarization on the nanopatterned porous titanium samples, the conformal nanopatterning inherent to DIS of complex porous titanium scaffolds has shown similar results as the methods mentioned above. The hierarchical micro/nanostructures modulated immune and bone cells without harsh reagents, coatings, or absorbed proteins. Thus, DIS has potential in modulating the osteoimmune environment, which could enhance the osseointegration process.

5 | CONCLUSIONS

DIS is an ion irradiation technique that uses argon ions to produce nanotopography in a fast, scalable, and conformal way. By controlling DIS variables, we can tailor the shape and orientation of nanofeatures, which in turn modulate cell functions. The current experimental results demonstrated that nanotextured porous commercially pure Ti scaffolds, sintered by powder metallurgy and modified by DIS, generated biocompatible surfaces that increased osteoblast ALP activity after 7 days. Calcium deposits increased on nanotextured porous scaffolds after 14 days. The porous structures cleared macrophages after 24 h and seemed to reduce the number of multinucleated cells on the irradiated surfaces. All these findings suggest that nanofeatures designed by DIS enhanced cellular interactions at the bio interface, improving Ti osseointegration.

AUTHOR CONTRIBUTIONS

The manuscript was written through contributions of all authors. Ana Civantos, Andrea Mesa-Restrepo, Yadir Torres, Akshath R. Shetty, Ming Kit Cheng, Camilo Jaramillo-Correa, Teresa Aditya, and Jean Paul Allain have given approval to the final version of the manuscript.

ACKNOWLEDGMENTS

We thank Materials Research laboratory (MRL), Holonyak Micro and Nanolaboratory (HMNTL), and Beckman Institute of University of Illinois at Urbana–Champaign (UIUC) for their facilities to perform surface characterization and in vitro experiments. We will also like to

thank Dr. Viviana Posada Perez for her useful insights and analysis for this paper.

FUNDING INFORMATION

This work was supported by the Ministry of Science and Innovation of Spain under the grant PID2019-109371GB-I00, by the Junta de Andalucía–FEDER (Spain) through the Project Ref. US-1259771 and strategic funding from University of Illinois at Urbana-Champaign and the Pennsylvania State University.

CONFLICT OF INTEREST STATEMENT

The authors declare the following financial interests/personal relationships "Jean Paul Allain is the co-founder and CSO of Editekk Inc." which may be considered as potential competing interests.

DATA AVAILABILITY STATEMENT

The data that support the findings of this study are available from the corresponding author upon reasonable request.

ORCID

Andrea Mesa-Restrepo https://orcid.org/0000-0001-7324-2105

REFERENCES

1. Koons GL, Diba M, Mikos AG. Materials design for bone-tissue engineering. *Nat Rev Mater*. 2020;5:584-603. doi:10.1038/s41578-020-0204-2
2. Civantos A, Martínez-Campos E, Ramos V, Elvira C, Gallardo A, Abarrategi A. Titanium coatings and surface modifications: toward clinically useful bioactive implants. *ACS Biomater Sci Eng*. 2017;3:1245-1261. doi:10.1021/acsbiomaterials.6b00604
3. García-Gareta E, Hua J, Orera A, Kohli N, Knowles JC, Blunn GW. Biomimetic surface functionalization of clinically relevant metals used as orthopaedic and dental implants. *Biomed Mater*. 2017;13:1-14. doi:10.1088/1748-605X/aa87e6
4. Chun HJ, Park K, Kim C-H, Khang G, eds. *Novel Biomaterials for Regenerative Medicine*. Springer Singapore; 2018. doi:10.1007/978-981-13-0947-2
5. Lascano S, Arévalo C, Montealegre-Melendez I, et al. Porous titanium for biomedical applications: evaluation of the conventional powder metallurgy frontier and space-holder technique. *Appl Sci*. 2019;9:1-13. doi:10.3390/app9050982
6. Ye B, Dunand DC. Titanium foams produced by solid-state replication of NaCl powders. *Mater Sci Eng A*. 2010;528:691-697. doi:10.1016/j.msea.2010.09.054
7. Chino Y, Dunand DC. Directionally freeze-cast titanium foam with aligned, elongated pores. *Acta Mater*. 2008;56:105-113. doi:10.1016/j.actamat.2007.09.002
8. Ortiz-Hernandez M, Rappe K, Molmeneu M, et al. Two different strategies to enhance osseointegration in porous titanium: inorganic thermo-chemical treatment versus organic coating by peptide adsorption. *IJMS*. 2018;19:2574. doi:10.3390/ijms19092574
9. Fang ZZ, Paramore JD, Sun P, et al. Powder metallurgy of titanium——past, present, and future. *Int Mater Rev*. 2018;63:407-459. doi:10.1080/09506608.2017.1366003
10. Torres Y, Pavón J, Trueba P, Cobos J, Rodriguez-Ortiz JA. Design, fabrication and characterization of titanium with graded porosity by using space-holder technique. *Procedia Mater Sci*. 2014;4:115-119. doi:10.1016/j.mspro.2014.07.610
11. Civantos A, Domínguez C, Pino RJ, et al. Designing bioactive porous titanium interfaces to balance mechanical properties and in vitro cells behavior towards increased osseointegration. *Surf Coat Technol*. 2019;368:162-174. doi:10.1016/j.surfcoat.2019.03.001
12. Domínguez-Trujillo C, Ternero F, Rodríguez-Ortiz JA, et al. Improvement of the balance between a reduced stress shielding and bone ingrowth by bioactive coatings onto porous titanium substrates. *Surf Coat Technol*. 2018;338:32-37. doi:10.1016/j.surfcoat.2018.01.019
13. Chimutengwende-Gordon M, Dowling R, Pendegrass C, Blunn G. Determining the porous structure for optimal soft-tissue ingrowth: an in vivo histological study. *PLoS One*. 2018;13:e0206228. doi:10.1371/journal.pone.0206228
14. Lin X, Patil S, Gao Y-G, Qian A. The bone extracellular matrix in bone formation and regeneration. *Front Pharmacol*. 2020;11:757. doi:10.3389/fphar.2020.00757
15. Biggs MJP, Richards RG, Dalby MJ. Nanotopographical modification: a regulator of cellular function through focal adhesions. *Nanomed Nanotechnol Biol Med*. 2010;6:619-633. doi:10.1016/j.nano.2010.01.009
16. Karazisis D, Ballo AM, Petronis S, et al. The role of well-defined nanotopography of titanium implants on osseointegration: cellular and molecular events in vivo. *Int J Nanomedicine*. 2016;11:1367-1382. doi:10.2147/IJN.S101294
17. Lyons JG, Plantz MA, Hsu WK, Hsu EL, Minardi S. Nanostructured biomaterials for bone regeneration. *Front Bioeng Biotechnol*. 2020;8:922. doi:10.3389/fbioe.2020.00922
18. Chen L, Wang D, Peng F, et al. Nanostructural surfaces with different elastic moduli regulate the immune response by stretching macrophages. *Nano Lett*. 2019;19:3480-3489. doi:10.1021/acs.nanolett.9b00237
19. Karazisis D, Omar O, Petronis S, Thomsen P, Rasmusson L. Molecular response to nanopatterned implants in the human jaw bone. *ACS Biomater Sci Eng*. 2021;7:5878-5889. doi:10.1021/acsbiomaterials.1c00861
20. Luo J, Walker M, Xiao Y, Donnelly H, Dalby MJ, Salmeron-Sanchez M. The influence of nanotopography on cell behaviour through interactions with the extracellular matrix——a review. *Bioact Mater*. 2022;15:145-159. doi:10.1016/j.bioactmat.2021.11.024
21. Chen Z, Ni S, Han S, et al. Nanoporous microstructures mediate osteogenesis by modulating the osteo-immune response of macrophages. *Nanoscale*. 2017;9:706-718. doi:10.1039/C6NR06421C
22. Li J, Zhou P, Attarilar S, Shi H. Innovative surface modification procedures to achieve micro/nano-graded Ti-based biomedical alloys and implants. *Coatings*. 2021;11:647. doi:10.3390/coatings11060647
23. Quinn J, McFadden R, Chan C-W, Carson L. Titanium for orthopedic applications: an overview of surface modification to improve biocompatibility and prevent bacterial biofilm formation. *iScience*. 2020;23:101745. doi:10.1016/j.isci.2020.101745
24. Maalouf M, Abou Khalil A, Di Maio Y, et al. Polarization of femtosecond laser for titanium alloy nanopatterning influences osteoblastic differentiation. *Nanomaterials*. 2022;12:1619. doi:10.3390/nano12101619
25. Yeo ISL. Modifications of dental implant surfaces at the micro- and nano-level for enhanced osseointegration. *Materials*. 2019;13:89. doi:10.3390/ma13010089
26. Kligman S, Ren Z, Chung C-H, et al. The impact of dental implant surface modifications on osseointegration and biofilm formation. *JCM*. 2021;10:1641. doi:10.3390/jcm10081641
27. Harawaza K, Cousins B, Roach P, Fernandez A. Modification of the surface nanotopography of implant devices: a translational perspective. *Mater Today Bio*. 2021;12:100152. doi:10.1016/j.mtbio.2021.100152
28. Allain JP, Nieto M, Hendricks MR, Plotkin P, Harilal SS, Hassanein A. IMPACT: a facility to study the interaction of low-energy intense

particle beams with dynamic heterogeneous surfaces. *Rev Sci Instrum*. 2007;78:113105. doi:10.1063/1.2805677

29. Allain JP, Echeverry-Rendón M, Pavón J, Arias S. Nanostructured biointerfaces. *Nanopatterning and Nanoscale Devices for Biological Applications*. Devices, Circuits, and Systems; CRC Press; 2014:41-72. doi:10.1201/b17161
30. Civantos A, Barnwell A, Shetty AR, et al. Designing nanostructured Ti6Al4V bioactive interfaces with directed irradiation synthesis toward cell stimulation to promote host–tissue-implant integration. *ACS Biomater Sci Eng*. 2019;5:3325-3339. doi:10.1021/acsbiomaterials.9b00469
31. Chu PK, Chen JY, Wang LP, Huang N. Plasma-surface modification of biomaterials. *Mater Sci Eng R: Rep*. 2002;36:143-206. doi:10.1016/S0927-796X(02)00004-9
32. Bazaka K, Jacob MV, Crawford RJ, Ivanova EP. Plasma-assisted surface modification of organic biopolymers to prevent bacterial attachment. *Acta Biomater*. 2011;7:2015-2028. doi:10.1016/j.actbio.2010.12.024
33. Allain JP, Shetty A. Unraveling atomic-level self-organization at the plasma-material interface. *J Phys D Appl Phys*. 2017;50:283002. doi:10.1088/1361-6463/aa7506
34. Norris SA, Aziz MJ. Ion-induced nanopatterning of silicon: toward a predictive model. *Appl Phys Rev*. 2019;6:011311. doi:10.1063/1.5043438
35. Norris SA. Ion-assisted phase separation in compound films: an alternate route to ordered nanostructures. *J Appl Phys*. 2013;114:204303. doi:10.1063/1.4833551
36. Chan WL, Pavenayotin N, Chason E. Kinetics of ion-induced ripple formation on Cu (001) surfaces. *Phys Rev B*. 2004;69:245413. doi:10.1103/PhysRevB.69.245413
37. Torres Y, Pavón JJ, Rodríguez JA. Processing and characterization of porous titanium for implants by using NaCl as space holder. *J Mater Process Technol*. 2012;212:1061-1069. doi:10.1016/j.jmatprotec.2011.12.015
38. ASTM International. ASTM F67-00. Standard specification for unalloyed titanium for surgical implant applications (UNS R50250, UNS R50400, UNS R50550, UNS R50700). 2002 https://webstore.ansi.org/Standards/ASTM/astmf6700
39. ASTM International. ASTM C373-14. Standard test method for water absorption, bulk density, apparent porosity, and apparent specific gravity of fired whiteware products, ceramic tiles, and glass tiles. 2014 https://webstore.ansi.org/standards/astm/astmc37314
40. ASTM International. ASTM E9-09. Standard test methods of compression testing of metallic materials at room temperature. 2018 https://www.astm.org/e0009-09.html
41. Allain JP, Barnwell A, Shetty AR, Fernandez Civantos AF, Torres Y, Pavon JJ. Nanostructured titanium-based compositions and methods to fabricate the same. US Patent *US20200149145A1*. 2020.
42. Allain JP, Pavon JJ, Torres Y, Shetty AR, Barnwell A. Nanostructured titanium-based compositions and methods to fabricate the same. US Patent 16/592,195. 2020.
43. Nabiee M, Fattah-alhosseini A, Mahmoudi A-H. Shot peening effects on corrosion behavior of commercial pure titanium in body simulating solution. *Mater Res Express*. 2019;6:116556. doi:10.1088/2053-1591/ab49a6
44. Bagherifard S, Fernández Pariente I, Ghelichi R, Guagliano M. Fatigue properties of nanocrystallized surfaces obtained by high energy shot peening. *Proc Eng*. 2010;2:1683-1690. doi:10.1016/j.proeng.2010.03.181
45. Torres Y, Lascano S, Bris J, Pavon J, Rodriguez JA. Development of porous titanium for biomedical applications: a comparison between loose sintering and space holder techniques. *Mater Sci Eng C*. 2014;37:148-155. doi:10.1016/j.msec.2013.11.036
46. Civantos A, Beltrán AM, Domínguez-Trujillo C, et al. Balancing porosity and mechanical properties of titanium samples to favor cellular growth against bacteria. *Metals*. 2019;9:9. doi:10.3390/met9101039
47. Civantos A, Allain JP, Pavón JJ, et al. Directed irradiation synthesis as an advanced plasma technology for surface modification to activate porous and "as-received" titanium surfaces. *Metals*. 2019;9:1349. doi:10.3390/met9121349
48. Posada VM, Civantos A, Ramírez J, Fernández-Morales P, Allain JP. Tailoring adaptive bioresorbable Mg-based scaffolds with directed plasma nanosynthesis for enhanced osseointegration and tunable resorption. *Appl Surf Sci*. 2021;550:149388. doi:10.1016/j.apsusc.2021.149388
49. Chen X, Fan H, Deng X, et al. Scaffold structural microenvironmental cues to guide tissue regeneration in bone tissue applications. *Nanomaterials*. 2018;8:960. doi:10.3390/nano8110960
50. Mesa-Restrepo A, Civantos A, Allain J, et al. Synergistic effect of rhBMP-2 protein and nanotextured titanium alloy surface to improve osteogenic implant properties. *Metals*. 2021;11:464. doi:10.3390/met11030464
51. Przekora A. The summary of the most important cell-biomaterial interactions that need to be considered during in vitro biocompatibility testing of bone scaffolds for tissue engineering applications. *Mater Sci Eng C*. 2019;97:1036-1051. doi:10.1016/j.msec.2019.01.061
52. Chen K, Jiao Y, Liu L, et al. Communications between bone marrow macrophages and bone cells in bone remodeling. *Front Cell Dev Biol*. 2020;8:598263. doi:10.3389/fcell.2020.598263
53. Xie Y, Hu C, Feng Y, et al. Osteoimmunomodulatory effects of biomaterial modification strategies on macrophage polarization and bone regeneration. *Regen Biomater*. 2020;7:233-245. doi:10.1093/rb/rbaa006
54. Martin KE, García AJ. Macrophage phenotypes in tissue repair and the foreign body response: implications for biomaterial-based regenerative medicine strategies. *Acta Biomater*. 2021;133:4-16. doi:10.1016/j.actbio.2021.03.038
55. Hotchkiss KM, Ayad NB, Hyzy SL, Boyan BD, Olivares-Navarrete R. Dental implant surface chemistry and energy alter macrophage activation *in vitro*. *Clin Oral Impl Res*. 2017;28:414-423. doi:10.1111/clr.12814
56. Padmanabhan J, Kyriakides TR. Nanomaterials, inflammation, and tissue engineering. *Wiley Interdiscip Rev Nanomed Nanobiotechnol*. 2015;7:355-370. doi:10.1002/wnan.1320
57. Ahmadzadeh K, Vanoppen M, Rose CD, Matthys P, Wouters CH. Multinucleated giant cells: current insights in phenotype, biological activities, and mechanism of formation. *Front Cell Dev Biol*. 2022;10:873226. doi:10.3389/fcell.2022.873226
58. Abbasi N, Hamlet S, Love RM, Nguyen N-T. Porous scaffolds for bone regeneration. *J Sci Adv Mater Dev*. 2020;5:1-9. doi:10.1016/j.jsamd.2020.01.007
59. Karageorgiou V, Kaplan D. Porosity of 3D biomaterial scaffolds and osteogenesis. *Biomaterials*. 2005;26:5474-5491. doi:10.1016/j.biomaterials.2005.02.002
60. Kapat K, Srivas PK, Rameshbabu AP, et al. Influence of porosity and pore-size distribution in Ti_6Al_4V foam on physicomechanical properties, osteogenesis, and quantitative validation of bone ingrowth by micro-computed tomography. *ACS Appl Mater Interfaces*. 2017;9:39235-39248. doi:10.1021/acsami.7b13960
61. Rosa AL, Crippa GE, De Oliveira PT, Taba M Jr, Lefebvre L-P, Beloti MM. Human alveolar bone cell proliferation, expression of osteoblastic phenotype, and matrix mineralization on porous titanium produced by powder metallurgy. *Clin Oral Implants Res*. 2009;20:472-481. doi:10.1111/j.1600-0501.2008.01662.x
62. Abagnale G, Steger M, Nguyen VH, et al. Surface topography enhances differentiation of mesenchymal stem cells towards osteogenic and adipogenic lineages. *Biomaterials*. 2015;61:316-326. doi:10.1016/j.biomaterials.2015.05.030
63. Tan G, Tan Y, Ni G, et al. Controlled oxidative nanopatterning of microrough titanium surfaces for improving osteogenic activity.

J Mater Sci Mater Med. 2014;25:1875-1884. doi:10.1007/s10856-014-5232-2

64. Markhoff J, Wieding J, Weissmann V, Pasold J, Jonitz-Heincke A, Bader R. Influence of different three-dimensional open porous titanium scaffold designs on human osteoblasts behavior in static and dynamic cell investigations. *Materials*. 2015;8:5490-5507. doi:10.3390/ma8085259
65. Xie K, Guo Y, Zhao S, et al. Partially melted Ti6Al4V particles increase bacterial adhesion and inhibit osteogenic activity on 3D-printed implants: an In vitro study. *Clin Orthop Relat Res*. 2019;477:2772-2782. doi:10.1097/CORR.0000000000000954
66. Ishak MI, Liu X, Jenkins J, Nobbs AH, Su B. Protruding nanostructured surfaces for antimicrobial and osteogenic titanium implants. *Coatings*. 2020;10:756. doi:10.3390/coatings10080756
67. Arias SL, Devorkin J, Spear JC, Civantos A, Allain JP. Bacterial envelope damage inflicted by bioinspired nanostructures grown in a hydrogel. *ACS Appl Bio Mater*. 2020;3:7974-7988. doi:10.1021/acsabm.0c01076
68. Padmanabhan J, Augelli MJ, Cheung B, et al. Regulation of cell-cell fusion by nanotopography. *Sci Rep*. 2016;6:33277. doi:10.1038/srep33277

SUPPORTING INFORMATION

Additional supporting information can be found online in the Supporting Information section at the end of this article.

How to cite this article: Civantos A, Mesa-Restrepo A, Torres Y, et al. Nanotextured porous titanium scaffolds by argon ion irradiation: Toward conformal nanopatterning and improved implant osseointegration. *J Biomed Mater Res*. 2023; 1-16. doi:10.1002/jbm.a.37582